Level0-to-Level1B processor for MethaneAIR

Eamon K. Conway[1,6], Amir H. Souri[1], Joshua Benmergui[2], Kang Sun[3,4], Xiong Liu[1], Carly Staebell[3], Christopher Chan Miller[1], Jonathan Franklin[2], Jenna Samra[1], Jonas Wilzewski[1], Sebastien Roche[1], Bingkun Luo[1], Apisada Chulakadabba[2], Maryann Sargent[2], Jacob Hohl[1], Bruce Daube[1], Iouli Gordon[1], Kelly Chance[1], and Steven Wofsy[2,5]

[1]Center for Astrophysics | Harvard and Smithsonian, Atomic and Molecular Physics Division, Cambridge, MA, USA
[2]Harvard John A. Paulson School of Engineering and Applied Sciences, Harvard University, Cambridge, MA, USA
[3]Department of Civil, Structural and Environmental Engineering, University at Buffalo, Buffalo, NY, USA
[4]Research and Education in Energy, Environment and Water Institute, University at Buffalo, Buffalo, NY, USA
[5]Department of Earth and Planetary Sciences, Harvard University, Cambridge, MA, USA
[6]Kostas Research Institute, Northeastern University, Burlington, MA, USA

Correspondence: Eamon K. Conway (e.conway@kri.neu.edu)

Abstract.

This work presents the development of the MethaneAIR Level0–Level1B processor, which converts raw L0 data to calibrated and georeferenced L1B data. MethaneAIR is the airborne simulator for MethaneSAT, a new satellite under development by MethaneSAT LLC, a subsidiary of the Environmental Defense Fund (EDF). MethaneSAT's goals are to precisely map over 80% of the production sources of methane from oil and gas fields across the globe to an accuracy of 2–4 ppb on 2 km^2 scale. Efficient algorithms have been developed to perform dark corrections, estimate the noise, radiometrically calibrate data, and correct stray-light. A forward model integrated into the L0–L1B processor is demonstrated to retrieve wavelength shifts during flight accurately. It is also shown to characterize the Instrument Spectral Response Function (ISRF) changes occurring at each sampled spatial footprint. We demonstrate fast and accurate orthorectification of MethaneAIR data in a three-step process: i) initial orthorectification of all observations using aircraft avionics, a simple camera model, and a medium resolution digital elevation map, followed by ii) registration of oxygen (O_2) channel grey-scale images to reference Multispectral Instrument (MSI) band 11 imagery via Accelerated-KAZE (A-KAZE) feature extraction and linear transformation, and similar co-registration of methane (CH_4) channel grey-scale images to the registered O_2 channel images, and finally iii) optimization of the aircraft position and attitude to the registered imagery and calculation of viewing geometry. This co-registration technique accurately orthorectifies each channel to the referenced MSI imagery. However, in the pixel domain, radiance data for each channel are offset by almost 150-200 across–track pixels (rows) and need to be aligned for the full physics or proxy retrievals where both channels are simultaneously used. We leveraged our orthorectification tool to identify tie points with similar geographic locations in both CH_4 and O_2 images in order to produce shift parameters in the across-track and along-track dimensions. These algorithms described in this article will be implemented into the MethaneSAT L0–L1B processor.

1 Introduction

Methane (CH_4) is a potent greenhouse gas that, despite having an atmospheric lifetime of approximately twelve years, almost one eight to that of carbon dioxide, it has approximately 26 times the global warming potential (GWP) of CO_2 over a 100 years time horizon. Over the first 20 years, methane has a GWP approximately 70-80 times that of CO_2 (Forster et al., 2007). Analysis carried out by Etheridge et al. (1998) on ice-core samples extracted in the Antarctic peninsula showed atmospheric methane concentrations have rapidly increased since the 1700s. These increases are predominantly anthropogenic, driven by industrialization and agricultural demand (Hmiel et al., 2020). In 2017, atmospheric levels of CH_4 averaged 1850 ppb, triple the eighteenth-century limits of approximately 650 ppb (Nisbet et al., 2019). Despite knowledge of its large atmospheric warming potential, except for a 'stabilization' period between 2000 and 2007, methane concentrations continue to increase (Turner et al., 2019). Preliminary results from the National Oceanic and Atmospheric Administration (NOAA) suggest that 2020 may have seen the largest increase in atmospheric methane concentrations since 1983 (NOAA, 2021).

Methane monitoring instruments such as TROPOMI (Veefkind et al., 2012) can detect emission plumes to a 12 ppb precision on a 7×5 km^2 scale (Pandey et al., 2019; Zhang et al., 2020) at nadir. TROPOMI's 2600 km swath provides daily global coverage, which greatly increases our knowledge of emission hot-spots on the Earth, but the coarse resolution makes it challenging to quantify and detect small-scale sources. MethaneSAT (MethaneSAT LLC) will be launched sometime in the first quarter of 2024, and the mission aims to precisely map over 80% of the production sources of methane from oil and gas fields across the globe to an accuracy of 2–4 ppb on 2 km^2 scale, with a native spatial resolution of 400 m $\times$ 100 m (along and across track respectively) at nadir, supporting the goal of reducing methane emissions from the oil and gas sector by 45% by the end of 2025. It will have two spectrometers on board, an oxygen (O_2) sensor, and a methane (CH_4) sensor, both of which will operate in the shortwave infrared region. Retrieving methane to this precision will require the instruments to be calibrated to a high level of accuracy. It is expected that a signal to noise ratio of approximately 1,000 will enable this to be achieved. The CH_4 sensor will observe between 1598 nm and 1683 nm, which encompass the CO_2 absorption features at approximately 1610 nm and the CH_4 features at approximately 1650 nm. The O_2 sensor will observe between 1249 and 1305 nm, encompassing the 'singlet-delta' O_2 $a^1\Delta_g$ - $X^3\Sigma_g^-$ band at approximately 1270 nm. The swath range will encompass approximately 200 km at an altitude of approximately 526 km, with $\approx$ 2000 pixels across the track, enabling the precise detection and identification of point source emissions.

It has been more common to use the oxygen A-band at 762 nm to determine the optical path length along the line of sight, with the SCanning Imaging Absorption spectroMeter for Atmospheric CHartographY (SCIAMACHY), Greenhouse Gases Observing Satellite (GOSAT), TROPOspheric Monitoring Instrument (TROPOMI) and Orbiting Carbon Observatory-2 (OCO-2) all observing this band. Many experimental measurements of this band have hence been carried out to improve the quality of spectroscopic information (Drouin et al., 2017, 2013), which include the observation of electric quadrupole transitions (Miller and Wunch, 2012). However, recent efforts using cavity ring down spectrometers have significantly improved the spectroscopic information of the singlet-delta band. Konefał et al. (2020); Tran et al. (2020) have shown that prior transition intensities were incorrect by between 1-3%, a non-negligible and important improvement for the MethaneSAT mission. MethaneSAT will

also need to model the airglow in this band, which can pose a challenge. However, despite this, recent advances in airglow simulations using SCIAMACHY data have used this band and excellent results are attainable (Sun et al., 2018; Bertaux et al., 2020), which show that this band can be used for satellite remote sensing of greenhouse gasses.

Airborne simulators provide an opportunity to develop and validate science algorithms prior to obtaining observation data from a forthcoming space-based instrument. Considering the NASA TEMPO (Tropospheric Emissions Monitoring of Pollution) (Zoogman et al., 2017) geostationary satellite mission that will operate in the visible and ultraviolet spectral regions, Geostationary Trace gas and Aerosol Sensor Optimization (Geo-TASO) (Leitch et al., 2014; Nowlan et al., 2016), Airborne Compact Atmospheric Mapper (ACAM) (Kowalewski and Janz, 2009; Lamsal et al., 2017; Nowlan et al., 2018) and GEOstationary Coastal and Air Pollution Events (GEO-CAPE) Airborne Simulator (GCAS) are examples of airborne simulators that have provided the resources to design and enhance the retrieval algorithms. In the SWIR, AVIRIS (Thompson et al., 2016), MAMAP (Gerilowski et al., 2011), GHOST (Humpage et al., 2018) and JAXA's airborne instrument (Kuze et al., 2020), have been utilized to retrieve methane emissions. The airborne simulator for MethaneSAT is appropriately named MethaneAIR and it includes two spectrometers scanning almost the same SWIR regions as MethaneSAT. Ten research flights have been completed in different parts of the US, with the final flight consisting of airglow observations. These research flights provided high-quality observation data to develop a fully automated MethaneAIR L0–L1B processor. The data sets have proved invaluable in developing science algorithms for MethaneSAT. Four additional research flights were performed in the Fall of 2022, but will not be considered in this paper.

Table 1. Shown below are the details for each MethaneAIR deployment, including destination and approximate length of observation

Flight	Date	Destination	Time (hrs)
RF01	20191108	CO Frontal Range	2.3
RF02	20191112	CO Frontal Range	3.6
RF03	20210728	CO Frontal Range	3.2
RF04	20210730	Permian	5.5
RF05	20210803	Permian	6.4
RF06	20210806	Permian	6.2
RF07	20210809	Permian	6.8
RF08	20210811	Salt Lake City & Uinta Basin	6.1
RF09	20210813	Bakken	7.3
RF10	20210816	Airglow	4.7

It is not uncommon for instrument properties such as wavelength registration and instrument line shape to slowly deviate away from the measurements recorded on the ground (Sun et al., 2017a, b; Voors et al., 2006; Cai et al., 2022). Such variations can be a result of the vibration during the initial launch of the instrument or from the differences between the environmental conditions encountered in the air (or space) versus the laboratory setup on the ground. It is therefore quite useful to routinely perform in-flight calibration measurements to monitor for any possible changes. For OCO-2, Sun et al. (2017b) analyzed the observed instrument line shape (ILS) and wavelength registration and compared these to the ground-based calibration measurements. Several line shape models were tested, super-Gaussian (Beirle et al., 2017), Gaussian, stretch/squeeze of the pre-flight ILS, and a hybrid mix of Gaussian functions (Liu et al., 2015). It was found that the flat-top nature of the OCO-2 ILS made the Gaussian function unsuitable, however, reasonable results were obtained with the other models. While the TROPOMI instrument has dedicated onboard calibration light sources (van Hees et al., 2018; Van Kempen et al., 2019), the

laboratory-measured wavelength calibration parameters (Kleipool et al., 2018) are not optimized in the L0–L1B processing, but rather during trace gas retrievals in the L1–L2 processing.

The MethaneAIR spectral calibration measurements have already been described in great detail by Staebell et al. (2021): Wavelength, radiometric and straylight properties, together with the instrument response function (ISRF), were derived for each of the CH$_4$ and O$_2$ spectrometers. The measured data have been implemented into the MethaneAIR L0–L1B processor. In this article, the development of the L0–L1B processor will be described in detail.

2 MethaneAIR

2.1 The MethaneAIR Instrument
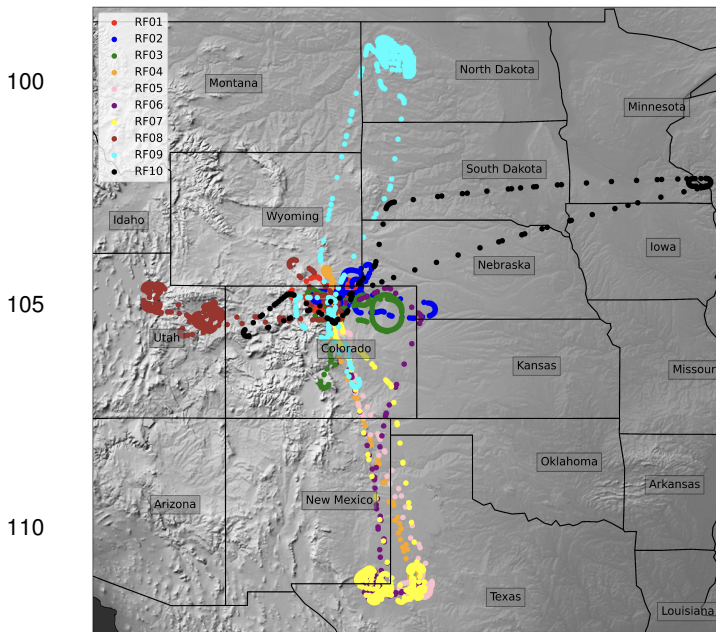
Figure 1. Map of the MethaneAIR research flights.

The MethaneAIR instrument closely echos the design of MethaneSAT. Two spectrometers, one measuring methane spectra and the other oxygen spectra, were integrated side-by-side onto the National Science Foundation (NSF) Gulfstream V (GV) aircraft that is controlled by the National Center for Atmospheric Research (NCAR) (NCAR - Earth Observing Laboratory, 2005). Each of these detectors possesses 1024 spectral pixels (columns) and 1280 spatial pixels (rows). The bandpass for the CH$_4$ sensor covers 1592–1680 nm, while the O$_2$ sensor spans 1236–1319 nm. Of the 1280 rows, only indices 135–997 and 308–1170 are illuminated in each of the respective CH$_4$ and O$_2$ sensors. The native spatial resolution of MethaneAIR observations is approximately 25 m (along-track) x 5 m (across-track) for a typical flight altitude of 9 km. More details of the MethaneAIR instrument are described by Staebell et al. (2021).

2.2 Research Flight Details

The dates, destinations, and observation times of the ten research flights we will consider in this paper are described in Table 1 and Figure 1. In total, approximately 50 hours of observation data were recorded for MethaneAIR. The first two flights, RF01 and RF02, which occurred in late 2019, were engineering flights, whose purpose was to ensure that the instrument was operating as expected. Over these two flights, 5.8 hours of observation data were collected in the Colorado Frontal Range. More flights were planned to occur at this time, however, flights ended due to GV maintenance issues and were rescheduled for
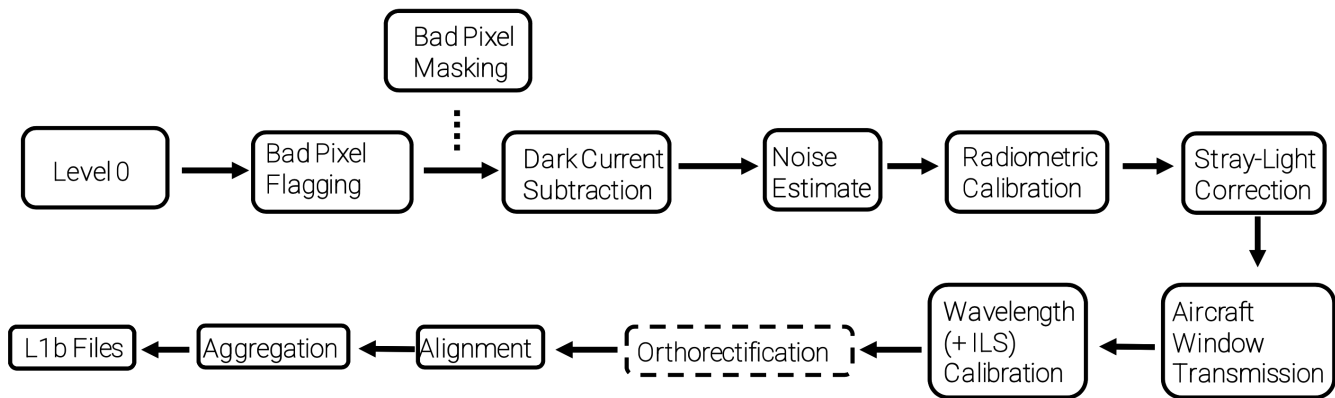
Figure 2. Flowchart representation of the processes within the MethaneAIR L0–L1B processor. The orthorectification process is in a dashed box to show that it is written in R code, and imported into Python.

a later date. Due to the COVID-19 outbreak, these rescheduled MethaneAIR flights were further delayed until the summer of 2021. Hence, these engineering flights proved to be critical contributors to the development of the science algorithms of both MethaneAIR and MethaneSAT.

RF03 was the first of these new flights and it covered a similar region as RF02. Its purpose was to validate both the instrument performance and science algorithms via comparisons to RF02, prior to mapping out targets encompassing oil and gas infrastructure. For RF04–RF07, MethaneAIR mapped out regions of the Permian Basin over the course of 25 hours (including transit time from Colorado). During RF04 and RF05 research flights, numerous passes over controlled methane release experiments also occurred. These releases provide valuable ground truth to evaluate our methane retrieval and emission estimate algorithms

Almost 6.1 hours of observation data were collected during RF08, which targeted Salt Lake City and the Uinta basin. For RF09, the Bakken oil and gas region that encompasses North Dakota was the designated target. For visual context, a map detailing the flight paths of RF01–RF09 is shown in Figure 1. RF10 was dedicated to investigating airglow emission, a key challenge for MethaneSAT's observations in the O_2 singlet-delta band. To measure airglow emission, the MethaneAIR payload was rotated 180 degrees so that the O_2 sensor could look vertically out of the upper port aboard the NCAR/GV aircraft.

3 L0–L1B Development

Figure 2 displays the processes of the L0–1B algorithm. Each processing step is described below from Sect. 3.1 through Sect. 3.8 and the process is fully automated. For 30 seconds of L0 data, which is the amount of time assigned to each individual observation granule (L0 file), the CPU time is approximately 90 minutes. Most of the run time is dedicated to the orthorectification procedures, primarily the final optimization procedure. The orthorectification procedure shown in Figure 2 is within a dashed enclosure as the process has two separate steps to it. The final one is a refinement procedure and is technically optional,

140 but provides more accurate geospatial information onto the pixels. The L0-L1B processes have also been configured to operate in a cloud environment, and for future flights of MethaneAIR, processing will be done in the cloud.

3.1 Dark Current and Bad Pixel Flagging

During each of the research flights, dark collects were obtained at different instances during the flights and each was used to filter bad pixels according to their standard deviation from the mean. By averaging together all frames in each of the 30-second

145 collects in the along-across direction, a mean dark current was derived and a 3-σ limit was used to identify the bad pixels, i.e. those pixels whose signals deviate from the mean by more than 3-σ. Applying this limit to each sensor, an average of 1617 and 467 bad pixels were identified in each of the O_2 and CH_4 sensors, respectively. Staebell et al. (2021) used a similar approach to flag bad pixels, using a 3-sigma deviation limit from the linear fit of the gain of each sensor.

These bad pixels were flagged/masked in all subsequent processes. Next, the mean dark current is subtracted from each

150 illuminated collect to yield dark corrected frames.

3.2 Noise Estimate

The XCH4 retrieval follows an optimal estimation framework adjusting the concentration of several absorbing trace gases and atmospheric states (i.e., temperature and pressure) to best match the observed radiance. The noise model determines the uncertainty of the observed radiance populating the covariance matrix of observations in the retrieval algorithm. Good

155 knowledge of the noise level is critical in reducing the contributions of observational errors to the retrieved XCH4. Using the dark collects, read noise (N_r) is calculated for each pixel by considering the standard deviation of the signal across the number of frames collected. Combining the mean dark current (D) in units of digital number (DN), measured raw signal (S) in DN, gain (g) in units of electrons/DN, the number of dark frames (N_f) with the electronic offset (ϵ) in DN, the noise (in DN) of a particular pixel is calculated via Eqn. 1. The electronic offset was determined to be 1,500 DN during the laboratory calibration

160 and is the dark signal expected for an integration time of zero. The CCD gain, defined as the slope of the variance to the median signal, was determined to be 4.6. These values will be converted to radiance and stored in the L1B files.

$$\frac{\sqrt{(S - \epsilon) * g + (\frac{D - \epsilon}{N_f}) * g + (N_r * g)^2}}{g} \tag{1}$$

3.3 Radiometric Calibration

Radiometric calibration converts raw sensor data in units of DN to radiance units. The radiometric calibration is based on labo-

165 ratory measurements using an integrating sphere with a calibrated broad band light source. A fifth-order polynomial is derived and subsequently applied to each illuminated pixel, whose coefficients originate (for RF01 and RF02) from the radiometric calibration measurements to convert DN to photons s^{-1} cm^{-2} nm^{-1} sr^{-1}. After the first two research flights were concluded, newer radiometric calibration files were created after an extensive calibration effort, using the same approach as Staebell et al. (2021). These newer coefficients were utilized in the processing of RF03–RF10. In situations where we have only a small

170 number of dark current collects for a research flight (less than two for RF01 and RF02), it can increase the possibility of ran-

dom telegraph signals (RTS) going unchecked if a second bad pixel filtering procedure is not implemented on the illuminated scenes. Hence, to screen for extreme outliers, any pixel with radiance over 10^{15} photons s^{-1} cm^{-2} nm^{-1} sr^{-1} or below 10^{10} photons s^{-1} cm^{-2} nm^{-1} sr^{-1} is also flagged as a bad pixel during processing. These limits were chosen as they are outside of the expected operating range of the sensors. In addition to the bad pixel map, two pixels were found to be problematic in the CH$_4$ channel of the first two research flights and were hence flagged. The radiometric calibration coefficients were identified to be the source of this error and were masked. None were captured in RF03–RF10, which used new calibration measurements.

3.4 Window Transmission

The GV was equipped with an anti-reflection coated window and for the wavelengths, we are interested in, 1236–1680 nm, the aircraft window transmittance changes smoothly from 99.7% to 98.1%. To account for the window transmittance, we divided the raw signal in DN by the transmittance.

3.5 Stray Light Correction

Stray light is undesirable electronmagnetic radiation that reaches the sensor and interferes with performance and can occur for various reasons. The MethaneAIR sensors were designed to minimize the presence of stray light. Ground-calibration efforts confirmed that less than 2% of the total light recorded by the sensors is traceable to stray light effects. A full description of the characterization of MethaneAIR stray-light kernels is described by Staebell et al. (2021), but we briefly describe it here. The stray light correction algorithm of Staebell et al. (2021), is based on the method used to correct the stray light in the TROPOMI instrument (Tol et al., 2018). The central region of 15 spectral $\times$ 11 spatial pixels of the stray light kernel is defined as in the band, and the kernel values in the central region are set to zero, so that and the stray light correction is applied to pixels outside of this central area. This modified kernel is referred to as the far-field kernel and was utilized in the stray light correction algorithm, where the light is iteratively deconvolved and redistributed.

3.6 Wavelength and ILS Calibration

Successful trace gas retrievals rely on accurate knowledge of the observed wavelength and the instrument line shape (ILS). Laboratory calibration efforts were carried out to measure these values pre-flight (Staebell et al., 2021); however, it is relatively common for the observed wavelength to deviate from the laboratory-calibrated measurements during operation. It is, therefore, necessary to supplement this process with a wavelength-fitting routine to adjust the coefficients during flight. Also, unlike TROPOMI, the MethaneAIR and MethaneSAT instrument configurations are not designed to allow us to accurately monitor the instrument line shape (ILS) during operation with calibrated on-board lasers. We therefore added a forward model into the L0–L1 processor that can reliably detect abrupt changes in the ILS during flight, however, this process is optional in the L0-L1B processor for MethaneAIR because precise inverse modelling occurs during the L1-L2 processing step where wavelength and ILS fitting parameters are retrieved. The forward model we consider begins with a high resolution (HR) (0.001 nm) solar spectrum $F_{solar}^{HR}(\lambda)$ (Coddington et al., 2021), where λ is the wavelength. The parameterization of λ with respect to spectral

pixel index is assumed throughout.

$$I(\lambda) = \int \underbrace{(e^{-\tau(\lambda+\lambda'+\delta\lambda)})^{HR}}_{A} \underbrace{F_{solar}(\lambda+\lambda'+\delta\lambda)^{HR}}_{B} \underbrace{L\left(\sum_i p_i(\lambda+\lambda'+\delta\lambda)\right)}_{C} d\lambda' \times \underbrace{\left(\sum_{k=0} Al_k \times (\lambda+\delta\lambda)^k\right)}_{D} + \underbrace{\sum_{j=0} B_j \times (\lambda+\delta\lambda)^j}_{E}$$

(2)

The first term in our forward model above, A, is the Lambert-Beer term that accounts for light attenuation in the atmosphere due to the presence of gases, which we will consider to be made up of water, methane, and oxygen. The next, B, is a high-resolution solar spectrum. C described the slit function or ILS, which is derived from parameters p_i. D is a polynomial scaling term and finally, E is a baseline correction term. The integration variable (λ') spans the wavelength range of the convolution. $\delta\lambda$ represents the wavelength shift. Al_k represents variables that are optimized in the fit, and scale the absorption factors (A, B, and C). B_j are also numerical values that are optimized and shift the observation.

For CH$_4$, cross sections are calculated from the line-by-line parameters in the HITRAN2020 (Gordon et al., 2021) database using the Voigt profile on a 0.001 nm grid for a variety of temperatures and pressures that cover the standard U.S. atmosphere ranges. For O$_2$-O$_2$ collision-induced absorption (CIA), we attempted to use several sources of data in our model, each of which is theoretically, experimentally or empirically derived. For theoretical CIA, we attempted to utilize the calculations from Karman et al. (2018), which we obtained from HITRANonline (Karman et al., 2019), for the experimental source, we tried to use the measurements from Maté et al. (1999), while we also considered the empirical TCCON CIA. For the absorbing species, the cross sections are weighted according to the standard US atmosphere with temperature (T) and pressure (P) at atmospheric layer i:

$$\sigma(\lambda) = \frac{\sum_i^{max} \sigma(\lambda, T_i, P_i) \times SCD_{geo}(T_i, P_i)}{\sum_i^{max} SCD_{geo}(T_i, P_i)}$$

(3)

where SCD_{geo} refers to the geometric slant column density.

The high-resolution data need to be convolved with respect to the measured ILS, which was probed at a number of wavelengths for both channels. For the methane channel, we have nine ISRF measurements at 1593 nm, 1600 nm, 1610 nm, 1620 nm, 1630 nm, 1640 nm, 1650 nm, 1660 nm, and 1670 nm, while for the oxygen channel we have ten measurements at 1254 nm, 1261 nm, 1268 nm, 1275 nm, 1282 nm, 1289 nm, 1296 nm, 1303 nm, 1310 nm and 1317 nm. The ILS at the unmeasured wavelengths was determined by interpolating the measured data points. The forward model has the option of fitting each ISRF using either a squeeze/stretch parameter applied to the LUT values, or a normalized Gaussian or super-Gaussian function. The parameters describing the slit function L are denoted as $p_i(\lambda)$ where the index runs over the number of possible parameters needed in each function for each ISRF: the Gaussian model has only one, squeeze/stretch has one while the super-Gaussian possesses two variables.

In Figure 3, the results of a single fit to observed O$_2$ and CH$_4$ spectra taken during RF01(a,c) and RF02(b,d) is demonstrated. In each case, 100 along track frames have been aggregated together to enhance the signal-to-noise ratio. In all cases, a third-order polynomial was used to fit a baseline, while a constant shift parameter was found to provide the best results. The retrieval
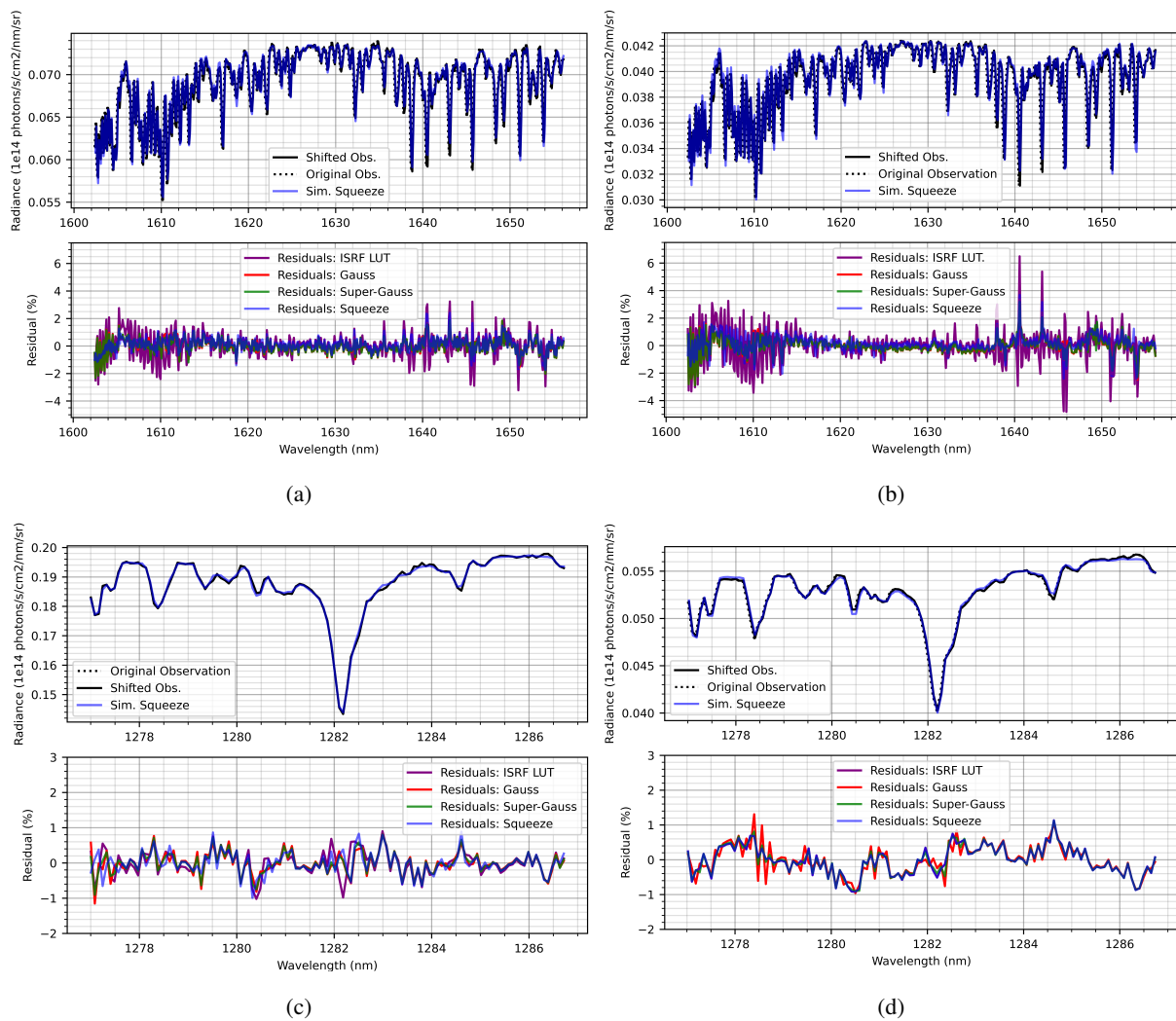
Figure 3. Example spectrum fits to RF01 and RF02 for CH_4 (a,b) and O_2 (c,d) channels respectively, using various ISRF models: laboratory measured values, Gaussian, super-Gaussian, and squeeze of ISRF LUT. Only the squeeze model simulation spectra are shown in the upper panels to enhance the visibility of the observed wavelength shift.

wavelength range will not be the same as the wavelength range considered for the derivation of the wavelength calibration in this process. This fitting procedure is to derive the wavelength shift that is occurring during flight, not to retrieve CH_4. The quantum efficiency of the instrument decreases towards the ends of the spectra and can increase the noise in the fit, hence the ends were omitted.

In Figures 3a and 3b, example fits in the CH_4 channel are presented for the engineering flights, RF01 and RF02. In both instances, modeling the ILS with a Gaussian, super-Gaussian, or squeeze/stretch term is shown to provide lower residuals when compared to a simulated spectrum using the initial look-up table of ISRFs, derived by Staebell et al. (2021). It is apparent that there are significantly lower residuals in RF01 than in RF02, and this can be explained by the cabin temperature not being controlled during RF02, and that the signal is higher in RF01. Analyzing both of these figures, it is quite clear that the measured ISRF FWHMs are too narrow. For the CH_4 band at 1630–1650 nm, the forward model can simulate the dominant observations with an average residual of 1–2% with either a Gaussian, super-Gaussian or squeeze model while using the LUT ISRFs yields residuals closer to 3-6% in the strong absorption features. At shorter wavelengths near 1605 nm, the residuals for the CO_2 band are within 1% with each of a Gaussian, super-Gaussian, or squeeze ISRF model.

For RF02, the wavelength was observed to shift between 0.12–0.15 nm throughout the flight, a large portion of which is likely due to the temperature variation on board. The shift is also cross-track dependent. For RF03, the wavelength shift was significantly larger, averaging 0.2 nm. The wavelength shifts for the remaining flights were significantly less, averaging approximately 0.01–0.05 nm. The derived wavelength shifts in all cases were rather insensitive to the choice of slit function used in the forward model.

For the oxygen singlet-delta band, simulating the strong Q branch was shown to be very problematic. Regardless of our choice of reference CIA data, or baseline polynomial, reasonable fitting results were not achievable using data from either research flight. We believe the difficulty is due to a combination of the CIA not being modelled correctly, large variations in the ISRF, and the simplicity of the forward model. Hence, we instead consider fitting the solar line at approximately 1282 nm and remove CIA as an absorbing species in the forward model. For each ISRF model considered, including the ISRF LUT values, residuals averaging less than 1% are attainable. This is true for all research flights. Example fits are shown for RF01 in Figure 3c and RF02, Figure 3d. For all flights, wavelength shifts in this channel are reasonably smaller than their CH_4 counterparts, averaging less than 0.05 nm.

The observed ISRF FWHMs for all research flights deviate from the laboratory-measured values from Staebell et al. (2021). As an example, we consider RF02, which was a flight where the variation is considerably large, evident from Figures 3a and 3b. Lower residuals are attainable for observations recorded in other research flights, likely a consequence of cabin temperature being controlled and monitored during flight, however, for RF02, the temperature was much less stable (not recorded). While this is clearly not an ideal situation for performing science retrievals, it does present the perfect opportunity to develop robust science algorithms.

The temperature variation in the aircraft cabin has likely resulted in the ILS changing throughout the RF02 flight. In Figure 4, the LUT ISRF data are fitted with a Gaussian line-shape and the resulting FWHMs are compared to the retrieved Gaussian FWHMs deduced from RF02 data at wavelengths: 1610 nm, 1620 nm, 1630 nm, 1640 nm, and 1650 nm. The results shown

are for a thirty-second granule captured when the aircraft was at 2.26 km and the granule consists of over 100 frames which were aggregated along–track. Dramatic changes in each ISRF are evident and differences of up to approximately 30% are observed in the FWHM. The pattern seems to be almost reversed with respect to the across–track dimension, evidence of large environmental changes surrounding the instruments on board. Despite these large variations, relatively low residuals are obtained during wavelength calibration.

3.7 Orthorectification

Orthorectification is the process of mapping camera projections onto the Earth's surface to accurately determine the geolocation of the measurements. In order to pinpoint the exact location of methane emission sources, retrievals of column-average mole fractions of methane (XCH_4) from MethaneAIR data have three major sensitivities to orthorectification accuracy:

1. The MethaneAIR instrument is composed of separate cameras for O_2 and CH_4 bands that must be spatially registered and aligned,

2. The retrieval algorithms require information about surface properties that vary widely over small spatial scales, and

3. The retrieval algorithms require information about the viewing geometry of the measurements.

The aim is to orthorectify the imagery to an accuracy of approximately 30 m, which is sufficient to pinpoint the emission source. Note that the sensitivity of the retrieval algorithms to the viewing geometry is not only a sensitivity to the camera projections onto the Earth's surface but also a sensitivity to the position and attitude of the camera itself. We apply an orthorectification procedure that makes a first guess using the aircraft avionics, then refines the mapping to the Earth's surface with an image registration algorithm, and finally refines the position and attitude of the cameras with a bundle adjustment algorithm.

Orthorectification requires a model of the camera position and attitude (the extrinsic model), a model of the camera pixel projections (the intrinsic model), and a model of the Earth's surface (a Digital Elevation Model or DEM).

Our first guess of the orthorectification uses an extrinsic model based on the aircraft's onboard avionics system. The onboard avionics system consists of two identical Honeywell LASEREF III/IV Inertial Reference Units (IRU) and a Garmin Model OEM WASS GPS-16 Unit (GPS) (NSF/NCAR Gulfstream V Investigator's Handbook, https://www.nasa.gov/pdf/594185main_gv_completehandbook.pdf). We use the position from the GPS-corrected IRU longitude and latitude, GPS altitude (altitude above mean sea level (MSL) plus the geoid height), and IRU true heading, pitch, and roll. These systems have a stated accuracy of ± 15m in horizontal position, ± 10m in vertical position, $\pm 0.05°$ pitch and roll, $\pm 0.2°$ in true heading. Sharp changes in attitude can affect the accuracy of the GPS unit and cause discontinuities in the aircraft position measurements. This was observed during the MethaneAIR flights. Additional attitude errors can result from the alignment and damping of the instrument mounting. As a result, our first guess orthorectification extrinsic model has substantially larger uncertainty than that reported in the avionics.

We apply a simple intrinsic model using a fixed focal length camera model with no distortion, distributing pixels at equal angles about the boresight ($2 \arctan(f \tan(\theta/2))$, where f is the focal length and θ is the field-of-view and is 33.7^o). MethaneAIR
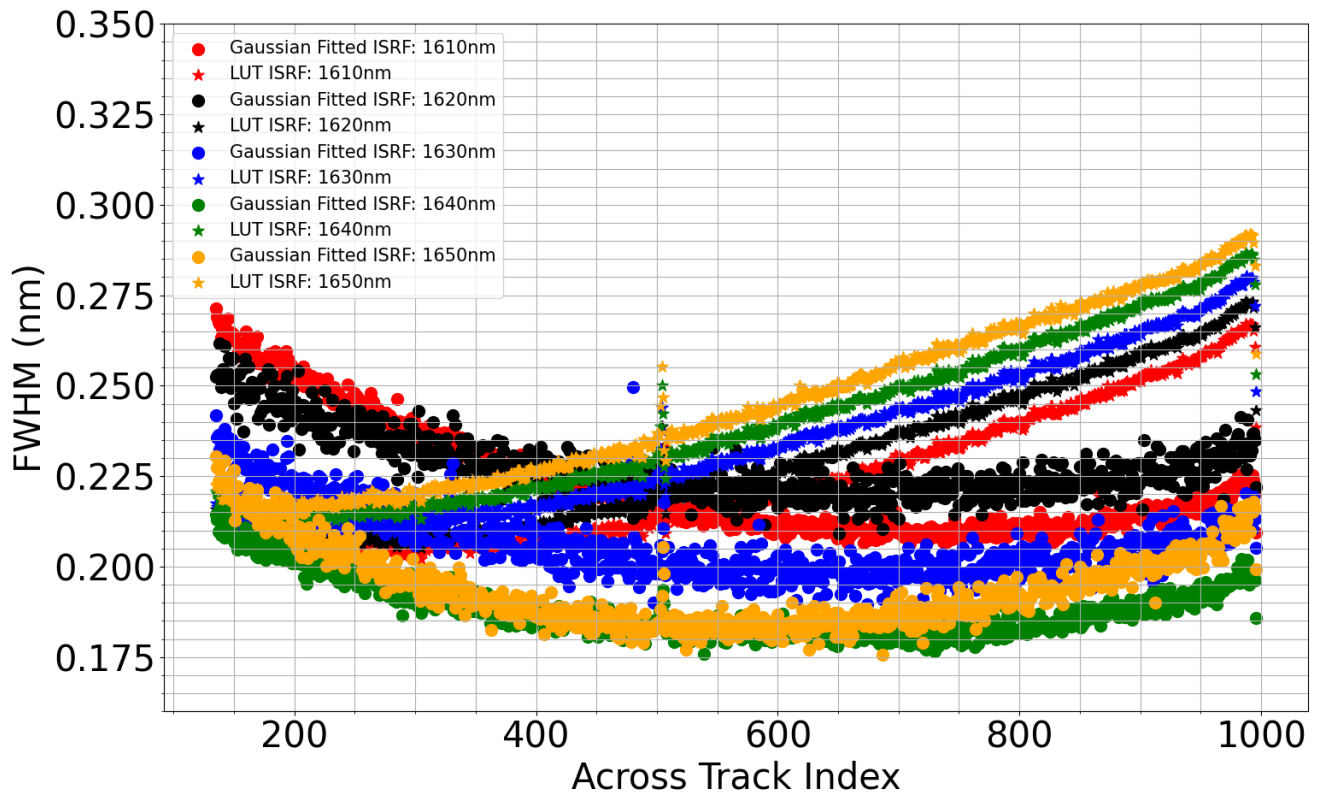
Figure 4. /blueRetrieved ISRF FWHM using a Gaussian model obtained from a 30-second granule in RF02 compared to the laboratory ISRF that was fit to a Gaussian for equal comparison.

used Edmund Optics 16 mm Focal Length Lens for 1" Sensor Format (https://www.edmundoptics.com/p/16mm-focal-length-lens-1quot-sensor-format/17861/). The lens has a reported TV distortion of < 1%.

DEM maps were created during processing using the United States Geological Survey (USGS) 3D Elevation Program (3DEP) 1 arc-second data, gathered via the Python `py3dep` package. To cover regions beyond the US for future flights we will replace this dataset by global ALOS DEM at 30 m resolution using our python `demalos` package (https://github.com/ahsouri/demalos)

The orthorectification algorithm proceeds as follows:

- – Calculate the aircraft position in meters in Earth-centered, Earth-fixed (ECEF) coordinate system from the longitude, latitude and elevation, assuming geodetic coordinates on the WGS84 ellipsoid.

- – Calculate unit vectors for the tangent frame to the WGS84 ellipsoid (North-East-Down) at the aircraft position.

- – Calculate unit vectors of the aircraft frame by applying intrinsic rotations to the tangent frame about the true heading, pitch, and roll.

- Calculate the camera boresight (assumed to be +z in the aircraft frame).

- Calculate individual pixel boresights by applying an additional rotation about the aircraft x axis according to the intrinsic model.

- Calculate reference vectors from each point on the DEM to the aircraft.

- Snap the pixel boresights to the reference vectors (i.e., find the closest reference vector using Euclidean distance in $\mathbf{R}^3$) to find the surface elevation for each pixel projection.

- Calculate the intersection of the pixel projection with an ellipsoid equal to the WGS84 ellipsoid adjusted to the surface elevation.

- Calculate the geodetic longitude and latitude of the intersection of the pixel projections with the Earth.

This algorithm's trade-off between speed and accuracy depends on the resolution of the DEM. When computing the orthorectification for output, we use the DEM with the full 1 arc second. When optimizing the aircraft position and attitude during bundle adjustment, we aggregate the DEM to 8 arc seconds (applied to the reprojection and the registered image).

We estimate the sun position using the Astronomical Almanac 2020 algorithm and transform from Earth-Centered Inertial (ECI) coordinate to ECEF by propagating through precession, nutation, Greenwich hour angle, and polar motion matrices using Earth orientation parameters from the International Earth Rotation and Reference Systems Service (IERS) Bulletin.

A fully automatic geometric correction, which refers to removing geometric distortions in raw images with respect to an orthogonal view of a reference image, is developed using a computer vision image registration method. We apply image registration to the avionics-based MethaneAIR imagery procedure in a two-step process: geographically matching i) the MethaneAIR O_2 imagery to cloud-free orthorectified Multispectral Instrument (MSI) (Sentinel-2) band 11 reflectance (1610 nm) at the top of the atmosphere and ii) CH_4 imagery to the rectified MethaneAIR O_2 imagery. We name the first (second) step as the absolute (relative) correction. In the first step, the use of the MethaneAIR O_2 channel is preferred over the CH_4 channel due to the presence of stronger signal-to-noise ratios. The clear-sky MSI imagery (<3% cloud in each scene covering 100×100 km^2) at the resolution of 20 m is taken at the nearest time with respect to that of the MethaneAIR acquisition enabling to minimize the potential differences in the surface features changing over time. We reduce the atmospheric interference by averaging the MethaneAIR radiance within the atmospheric windows of 1250-1255 nm and 1620-1630 nm for O_2 and CH_4, respectively. To be able to automatically extract distinctive points (called key-points) from the images, we leverage a multi-scale feature extraction method called Accelerated KAZE (A-KAZE) (Alcantarilla et al., 2013). This method uses a scale-based non-linear diffusion filter to describe distinctive features (i.e., corners, lines, patterns, etc.) while reducing noise and simultaneously retaining the boundaries of objects. An adaptive histogram equalizer with a window of 8x8 is used to enhance the image contrast, which is found to be advantageous in increasing the number of key-points. Subsequently, A-KAZE determines extrema by comparing filtered images by the diffusion filter at different scales (i.e., less to more blurred) in a window of 3×3 pixels. Low contrast key-points are eliminated by fitting a 2D quadratic function. Each key-point is then described by a 3-bit descriptor

encapsulating radiance intensity and vertical and horizontal gradients pertaining to patches neighboring the key-point based on Modified-Local Difference Binary (M-LDB) described in Alcantarilla et al. (2013). It is worth noting that each patch is defined based on the gradient vector, which in turn, makes the algorithm invariant to scale and rotation. We score the Hamming distance

345 between key-points generated from both MSI and MethaneAIR, remove the irrelevant features based on a fixed threshold, and use a brute-force matcher to pair them. A robust outlier detector called Random Sample Consensus (RANSAC) is applied to the paired key-point candidates with more than 10,000 iterations and a residual error threshold of $0.0005°$. This algorithm ultimately provides a linear relationship between the geographic latitudes and longitudes of the paired key-points extracted from the target (unrectified) image with respect to those from the reference one. This linear relationship mathematically explains

350 varying scales and translations between two images, allowing for rectifying major geometric misalignment. This algorithm is called GeoAKAZE, which is publicly available at (Souri, 2022).

In terms of the absolute correction, we run the geolocation algorithm on the entire set of MethaneAIR flights without suboptimally modifying the parameters defined in the algorithm, including the number of the RANSAC iteration and the size of the histogram equalizer window. The approach was found to be successful, with the results displayed in Table 2. These

355 numbers are estimated based on assessing individual paired images and considering the residuals obtained from the linear fit. The relatively poor performance in the RF01 data likely arises from a combination of the aircraft's low altitude and/or passes over mountainous terrain. Figure 5a depicts some instances of excellent proficiency of the method in orthorectifying the MethaneAIR O_2 images to MSI, while Figure 5b shows examples of the respective mapping of CH_4 to O_2. The background picture for (a) is taken from the MSI band 11 (the reference image), and the overlaid picture is from MethaneAIR O_2, while

360 for (b), the background is O_2. It is readily evident that features such as roads, farms, and buildings are better lined up after the corrections.

The spatial error associated with the avionics-only orthorectification data is depicted in a whisker-plot image; see Figure 6. RF01 has the largest range of errors of any flight, perhaps due to variable flight height and maneuver (Table 2). Except for this flight, the mean value of the median spatial error across the flights is approximately 600 m which is over an order of magnitude

365 greater than the native pixel resolution. This necessitated our need to implement the GeoAKAZE procedure to all flight data.

As for the relative correction, the success rates are found to consistently be over 95% for all the research flights of MethaneaAIR (not shown in Table 2). Since MethaneAIR O_2 and CH_4 radiances are captured at (nearly) the same time, geometry, and environment, we observe higher success rates compared to the absolute correction, indicating a strong degree of relevancy between the radiances.

370 Following this, we attempt to optimize the aircraft avionics (position and attitude of the aircraft) to the GEOAkaze-corrected pixel projections to produce optimized viewing geometry. The optimized avionics result in values of the viewing zenith angle, scattering angle, geometric airmass factor, etc., consistent with the observed imagery. We use the Limited-memory Broyden-Fletcher-Goldfarb-Shanno algorithm over a bounded domain (Byrd et al., 1995) to derive the corrections to the aircraft position (m ECEF) and attitude (degrees pitch, roll, true heading) that produces the minimum difference between the pixel projections

375 and the GEOAkaze-corrected pixel projections. In cases where the optimized correction falls near the edge of the domain (initialized to 200m or 10 degrees in each direction), we note the case for quality control checks and expand the domain

Table 2. Statistics from the orthorectification GeoAKAZE procedure for the MethaneAIR (M-AIR) research flights.

	A-KAZE Statistics			Reasons for failures		
Flight	Total Cases	Success	Failure	Clouds	Bad M-AIR Data	Missing/Irrelevant MSI
RF01	199	135 (68%)	64 (32%)	0 (0%)	42 (66%)	22 (34%)
RF02	358	314 (88%)	44 (12%)	0 (0%)	3 (7%)	41 (93%)
RF03	611	523 (85%)	88 (15%)	30 (34%)	22 (25%)	36 (41%)
RF04	190	164 (86%)	26 (14%)	13 (50%)	4 (15%)	9 (35%)
RF05	248	240 (97%)	8 (3%)	0 (0%)	0 (0%)	8 (100%)
RF06	318	301 (95%)	17 (5%)	1 (6%)	7 (41%)	9 (53%)
RF07	511	491 (96%)	20 (4%)	1 (5%)	7 (35%)	12 (60%)
RF08	404	381 (94%)	23 (6%)	0 (0%)	7 (30%)	16 (70%)
RF09	774	578 (75%)	196 (25%)	101 (52%)	43 (22%)	52 (26%)

and recompute the optimization. We compute the optimization independently for each data granule. This may result in small discontinuities in the orthorectification within the tolerance of the orthorectification error.

When the GEOAkaze process fails, the orthorectification optimization procedure cannot occur. Therefore, the L1B data uti-
380 lizes the less accurate avionics-only orthorectification data, which is always available. On the contrary, where the GeoAKAZE is successful, it is still possible for the optimization procedure to fail, either due to the optimizer failing to converge or if the av-erage deviation between the resulting optimized spatial positions and the GeoAKAZE positioning is greater than some defined threshold (which was 25 m for all flights; hence this is the upper bound on the orthorectification optimization accuracy against the GEOAkaze results). In such cases, we utilize the GeoAKAZE-derived longitude/latitude values in the main L1B Geolo-
385 cation group together with the avionics viewing geometries. We place the unsuccessful optimized values in a supporting data group for completeness. In the much more desirable situations where the optimization succeeds, we place the optimized data in the main group and the less accurate avionics data into a supporting group. The results of the orthorectification procedure are, thus, variable; hence, the dashed enclosure applied to the procedure is shown in Figure 2.

As for the failed cases in both absolute and relative geometric corrections, we design a simple and fast empirical method
390 to reduce their geometric offsets as much as possible by leveraging the successful cases from GeoAKAZE. This method finds a failed segment and nudges it towards the neighbouring successful segments by fitting a linear transformation between their coordinates at the extremities of along-track pixels. The method is carried out iteratively until no further unsuccessful segment exists.

3.8 Alignment Between the O_2 and CH_4 Channels in the Pixel Domain

395 The observed radiance frames of O_2 and CH_4 for the MethaneAIR instrument are not aligned in the across–track and along–track (image) dimensions. This was primarily caused by a boresight offset between two detectors (approximately 25 pixels)
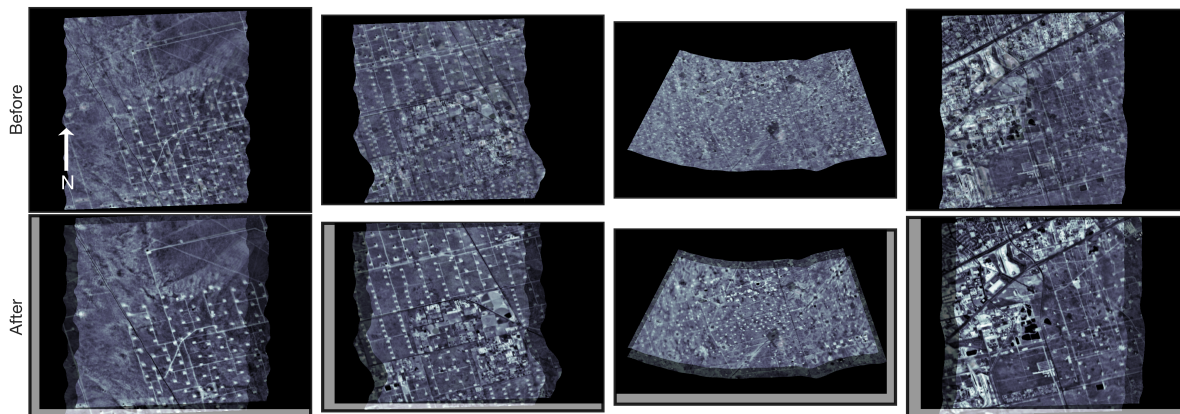
(a)
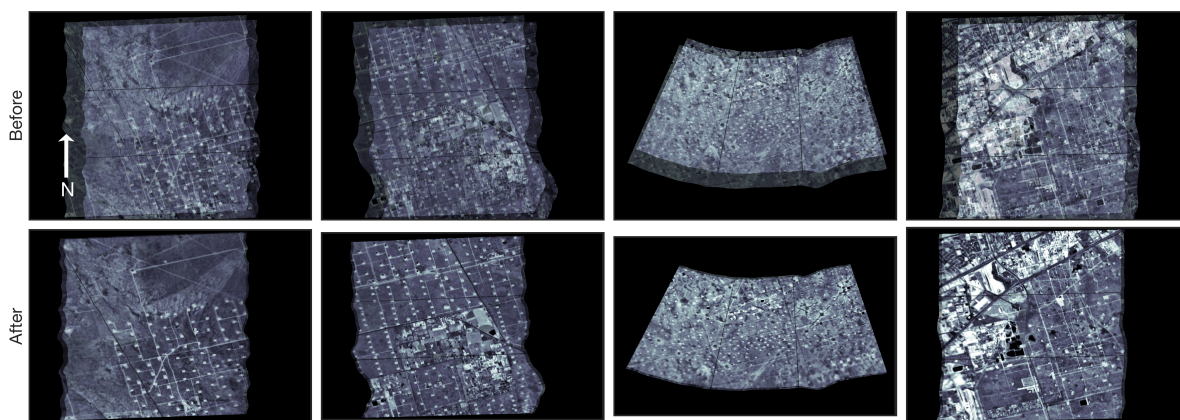
(b)

Figure 5. Shown in (a) are MSI band 11 imagery (background) overlaid by the spectrally-averaged MethaneAIR O_2 channel (foreground) before applying the geolocation correction (first row) and after (second row). In (b), spectrally-averaged MethaneAIR CH_4 channel (foreground) overlays spectrally-averaged MethaneAIR O_2 channel data (background) before applying the geolocation correction (first row) and after (second row). Note that surface features are markedly aligned between images after the adjustment.

and the fact that the sensors were orientated at 180° to each other. While the geolocation and viewing geometry parameters for each granule have been corrected to line up with each band, the offset needs to be determined in the pixel domain so that the ISRF table indices can be well incorporated in the full physics retrieval algorithm where both channels are simultaneously involved. The effective area of the spectrometers does not encompass the full 1,280 rows, but rather a subset of this, due to the design of the instrument. This can be seen in Figure 7 below.

An example of the offset is presented within Figure 7 (a), for O_2 (background) and CH_4 (foreground), respectively, where the radiance has been converted to grayscale units. This was done by averaging the radiance data in the wavelength ranges
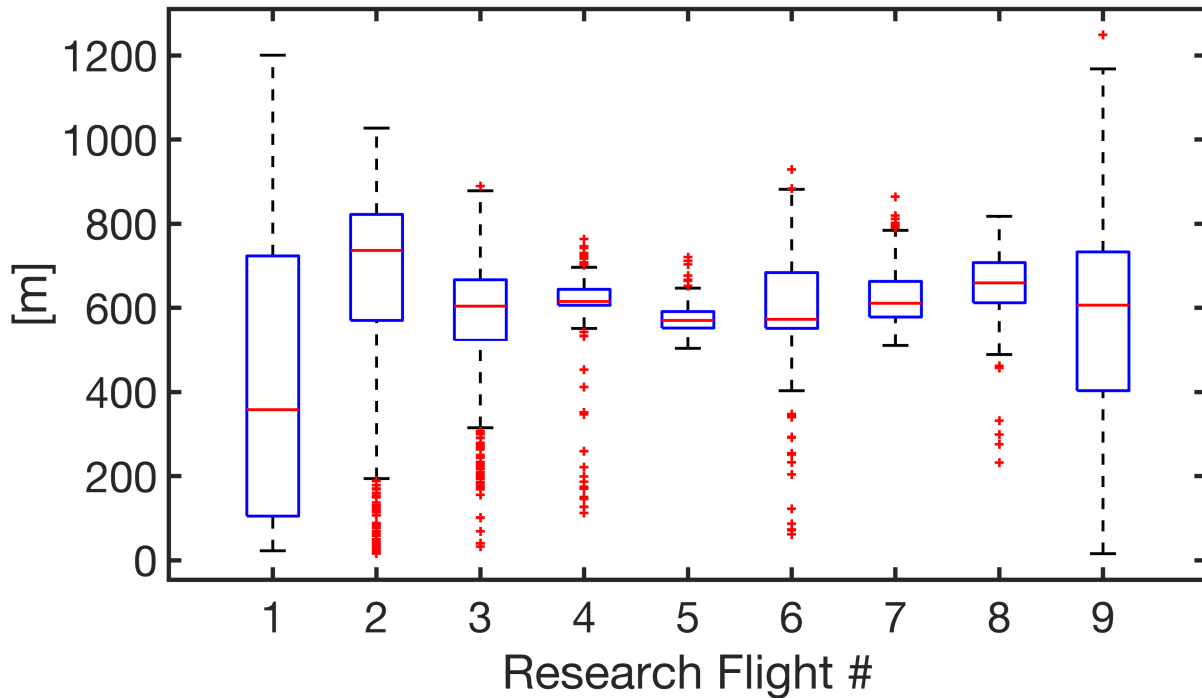
Figure 6. The box-whisker plots of geolocation errors (avionics-only orthorectification data) before the corrections. These plots are based on the succeeded cases from GeoAKAZE. On each box, the central red line shows the median, and the top and bottom edges of the box show the 25th (q1) and 75th (q3) percentiles. The dark solid lines at the very beginning and the end of each plot show the minimum and maximum values. Red plus symbols indicate outliers that are determined by any value above $q3 + 1.5 \times (q3 - q1)$ or below $q1 - 1.5 \times (q3 - q1)$.

of 1602–1638 nm and 1245–1273 nm for the CH_4 and O_2 sensors, respectively, normalizing these averages to the maximum
405   observed value in each, scaling by a factor of 255, and then applying the adaptive histogram equalization. Performing a full physics retrieval on such data will not be possible where pixel $[i, j]$ (in terms of along and across dimensions) of the O_2 channel does not align with pixel $[i, j]$ of the respective CH_4 granule.

Approximate 30 seconds of L0 data streams are processed into smaller granules of 10 seconds, and in particular instances, it is possible that there is an offset along–track (number of frames) of respective CH_4 and O_2 granules. The offset along the track
410   is very subtle, often less than 1–2 frames, but across the track the offset is large, evident from Figures 7 (a) and (b).

To deduce the offset corrections, we leveraged the GeoAKAZE relative correction parameters to set a mesh grid of tie points having identical latitudes and longitudes between two channels. Because the relative correction has co-registered these two bands with respect to each other and this process is irrespective of the performance of the absolute correction, these tie points should be legitimate choices to co-register two images in the image domain. This approach also reduces the computational
415   costs associated with running A-KAZE because it leverages the correction parameters made during the relative correction thus
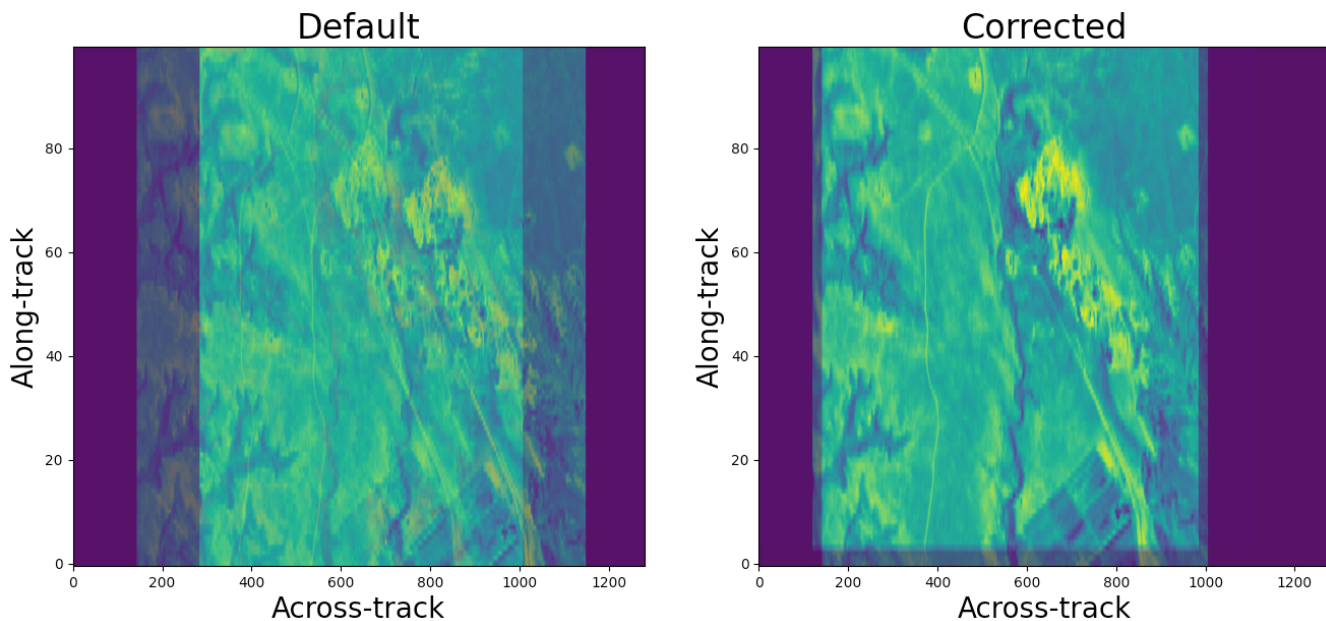
Figure 7. An example of the alignment offsets in respectively timestamped CH_4 (foreground) and O_2 (background) granules of ten seconds in length, procured during RF08. (left) The original radiance images, (right) The overlaid and aligned CH_4 and O_2 radiance images.

we are no longer required to recall A-KAZE. We identify the $[i, j]$ of the tie points and estimate two offsets, i.e. the offset pixel numbers in each dimension. In Figure 7 (b), the corrected CH_4 gray scale image is shown. For this, an along-track shift of three frames and an across–track shift of 163 were deduced to match two images in the image space. In general, the across–track and along–track shifts were found to be 192 ± 15pixel and 1 ± 1pixel for RF01 and RF02. While the along-track offset remained the same for other flights, the across-track shift was reduced to 159 ± 5pixel due to the O_2 camera being physically remounted onto the O_2 after RF03.

3.9 Aggregation

The signal-to-noise ratio (SNR) for individual pixels at the native resolution is approximately 90 and 140 for the CH_4 and O_2 spectrometers, respectively, which can sometimes be too low for accurately performing retrieval studies. To address this, the native resolution L1B files are supplemented with aggregated L1B data. We aggregated the native data into five segments across–track pixels (5×1). By performing this, the SNR is boosted by a factor of 2.2 for a 5×1 aggregation.

4 Conclusion

The mission goal of MethaneSAT is to precisely map over 80% of the production sources of methane emissions from oil and gas fields across the globe to an accuracy of 2–4 ppb on 2 km^2 scale. Accomplishing this task requires processing L0 data

streams to L1B products with high accuracy. The MethaneAIR airborne simulator has provided critical science data to develop mature and efficient algorithms that will be utilized in the L0–L1B processor for MethaneSAT. Within the observation data of the MethaneAIR research flights, several corrections were required to be developed.

Bad pixels are flagged by considering their standard deviation from the mean dark current, collected at numerous intervals throughout each flight. Stray light was corrected by following the results of Staebell et al. (2021), where a far field kernel is utilized to redistribute light outside of a 15×11 spectral-spatial window.

A forward model was developed using the latest available spectroscopic data from HITRAN2020. These were combined with a high-resolution solar spectrum and laboratory calibration data for both oxygen and methane sensors. A small increase in cabin temperature which occurred during the second research flight of MethaneAIR caused the instrument line shape to deviate from the laboratory-measured values, which became evident during wavelength calibration. The temperature increase was approximately 3-4 Kelvin. The forward model is demonstrated to accurately capture in-flight modulation of both the wavelength shift and ILS to a reasonable degree of accuracy.

To project MethaneAIR radiance observations onto the Earth's surface (orthorectification), we trace light rays from the instrument, through a camera model, to the surface topography. The orthorectification procedure is subject to errors on the order of 600-800 m, due primarily to uncertainty in the position and attitude of the camera. The orientation of each spectrometer relative to the aircraft avionics system will be a consistent 3-D rotation that can improve the accuracy of the initial first-guess derivation of the longitude and latitude of the L1B files. In future iterations, we will investigate this 3-D correction to improve the efficiency of the L0–L1B processing. To correct these errors, we register MethaneAIR O_2 band radiances to existing geo-referenced MSI band 11 imagery using a fully-automated feature extraction method called A-KAZE. We then apply the same algorithm to register MethaneAIR CH_4 band radiances to MethaneAIR O_2 band radiances. We then optimize the aircraft position and each camera's attitude to best fit the registered data (reprojection). Surface features in the ortho-rectified images in both flights are well aligned, suggesting significant improvements in the geolocation accuracy for most scenes (>90%). Nonetheless, we are aware of two important limitations of this approach which are i) the presence of cloud and ii) a long lag between the acquisition time of MSI and MethaneAIR for some cases due to our stringent cloud screening cut-off value resulting in unmatchable key-points. This automatic algorithm, named GeoAKAZE is publicly available (Souri, 2022) and can be used for other airborne missions.

The misalignment of the radiance data recorded by the methane and oxygen sensors initially makes them unsuitable to be used in the full physics retrieval algorithms, which requires the use of both channels. By converting the radiance data to grey-scale images, we demonstrate via the use of the relative correction parameters made by A-KAZE algorithm that the offsets (in pixel space) between the two sensors can be deduced to high accuracy and reliability. In this approach, the methane data were aligned to the oxygen sensor's data, and frames were added or subtracted to create a full matching set of data when necessary. This misalignment is expected to be much smaller for MethaneSAT.

The MethaneSAT L0–L1B processor will include all the algorithms described in this article, although not all may be required, and some may need to be modified.

Code and data availability. The L0-L1B processor and data are available upon request.

465   *Financial support.* This research was funded by MethaneSAT LLC and an NSF EAGER grant.

Author contributions. EC, AS, JB, KS, CS, BL developed scientific algorithms. JW, SR, CCM and AC contributed to algorithm design. IG contributed towards the spectroscopic data. JS, MS, JH and BD provided expertise on instrument design. XL, JF, KL and SW provided oversight on the campaign flight plans, algorithm designs and overall project guidance.

Competing interests. The authors declare that they have no conflict of interest.

470 References

Alcantarilla, P., Nuevo, J., and Bartoli, A.: Fast Explicit Diffusion for Accelerated Features in Nonlinear Scale Spaces, in: Procedings of the British Machine Vision Conference 2013, British Machine Vision Association, https://doi.org/10.5244/c.27.13, 2013.

Beirle, S., Lampel, J., Lerot, C., Sihler, H., and Wagner, T.: Parameterizing the instrumental spectral response function and its changes by a super-Gaussian and its derivatives, Atmospheric Measurement Techniques, 10, 581–598, https://doi.org/10.5194/amt-10-581-2017, 2017.

475 Bertaux, J.-L., Hauchecorne, A., Lefèvre, F., Bréon, F.-M., Blanot, L., Jouglet, D., Lafrique, P., and Akaev, P.: The use of the 1.27 µm O_2 absorption band for greenhouse gas monitoring from space and application to MicroCarb, Atmospheric Measurement Techniques, 13, 3329–3374, https://doi.org/10.5194/amt-13-3329-2020, 2020.

Byrd, R. H., Lu, P., Nocedal, J., and Zhu, C.: A Limited Memory Algorithm for Bound Constrained Optimization, SIAM Journal on Scientific Computing, 16, 1190–1208, https://doi.org/10.1137/0916069, 1995.

480 Cai, Z., Sun, K., Yang, D., Liu, Y., Yao, L., Lin, C., and Liu, X.: On-Orbit Characterization of TanSat Instrument Line Shape Using Observed Solar Spectra, Remote Sensing, 14, https://doi.org/10.3390/rs14143334, 2022.

Coddington, O. M., Richard, E. C., Harber, D., Pilewskie, P., Woods, T. N., Chance, K., Liu, X., and Sun, K.: The TSIS-1 Hybrid Solar Reference Spectrum, Geophysical Research Letters, 48, e2020GL091 709, https://doi.org/https://doi.org/10.1029/2020GL091709, 2021.

Drouin, B. J., Yu, S., Elliott, B. M., Crawford, T. J., and Miller, C. E.: High resolution spectral analysis of oxygen. III. Laboratory investigation

485 of the airglow bands, The Journal of Chemical Physics, 139, 144 301, https://doi.org/10.1063/1.4821759, 2013.

Drouin, B. J., Benner, D. C., Brown, L. R., Cich, M. J., Crawford, T. J., Devi, V. M., Guillaume, A., Hodges, J. T., Mlawer, E. J., Robichaud, D. J., Oyafuso, F., Payne, V. H., Sung, K., Wishnow, E. H., and Yu, S.: Multispectrum analysis of the oxygen A-band, Journal of Quantitative Spectroscopy and Radiative Transfer, 186, 118–138, https://doi.org/https://doi.org/10.1016/j.jqsrt.2016.03.037, satellite Remote Sensing and Spectroscopy: Joint ACE-Odin Meeting, October 2015, 2017.

490 Etheridge, D. M., Steele, L. P., Francey, R. J., and Langenfelds, R. L.: Atmospheric methane between 1000 A.D. and present: Evidence of anthropogenic emissions and climatic variability, Journal of Geophysical Research: Atmospheres, 103, 15 979–15 993, https://doi.org/https://doi.org/10.1029/98JD00923, 1998.

Forster, P., Ramaswamy, V., Artaxo, P., Berntsen, T., Betts, R., Fahey, D., Haywood, J., Lean, J., Lowe, D. C., Myhre, G., Nganga, J., Prinn, R., Raga, G., Schulz, M., and Dorland, R. V.: 2007: Changes in Atmospheric Constituents and in Radiative Forcing, 2007.

495 Gerilowski, K., Tretner, A., Krings, T., Buchwitz, M., Bertagnolio, P. P., Belemezov, F., Erzinger, J., Burrows, J. P., and Bovensmann, H.: MAMAP – a new spectrometer system for column-averaged methane and carbon dioxide observations from aircraft: instrument description and performance analysis, Atmospheric Measurement Techniques, 4, 215–243, https://doi.org/10.5194/amt-4-215-2011, 2011.

Gordon, I. E., Rothman, L. S., Hargreaves, R. J., Hashemi, R., Karlovets, E. V., Skinner, F. M., Conway, E. K., Hill, C., Kochanov, R. V., Tan, Y., Wcisło, P., Finenko, A. A., Nelson, K., Bernath, P. F., Birk, M., Boudon, V., Campargue, A., Chance, K. V., Coustenis, A., Drouin,

500 B. J., Flaud, J.-M., Gamache, R. R., Hodges, J. T., Jacquemart, D., Mlawer, E. J., Nikitin, A. V., Perevalov, V. I., Rotger, M., Tennyson, J., Toon, G. C., Tran, H., Tyuterev, V. G., Adkins, E. M., Baker, A., Barbe, A., Canè, E., Császár, A. G., Dudaryonok, A., Egorov, O., Fleisher, A. J., Fleurbaey, H., Foltynowicz, A., Furtenbacher, T., Harrison, J. J., Hartmann, J.-M., Horneman, V.-M., Huang, X., Karman, T., Karns, J., Kassi, S., Kleiner, I., Kofman, V., Kwabia–Tchana, F., Lavrentieva, N. N., Lee, T. J., Long, D. A., Lukashevskaya, A. A., Lyulin, O. M., Makhnev, V. Y., Matt, W., Massie, S. T., Melosso, M., Mikhailenko, S. N., Mondelain, D., Müller, H. S. P., Naumenko, O. V., Perrin,

505 A., Polyansky, O. L., Raddaoui, E., Raston, P. L., Reed, Z. D., Rey, M., Richard, C., Tóbiás, R., Sadiek, I., Schwenke, D. W., Starikova, E., Sung, K., Tamassia, F., Tashkun, S. A., Auwera, J. V., Vasilenko, I. A., Vigasin, A. A., Villanueva, G. L., Vispoel, B., Wagner, G.,

Yachmenev, A., and Yurchenko, S. N.: The HITRAN2020 molecular spectroscopic database, Journal of Quantitative Spectroscopy and Radiative Transfer, p. 107949, https://doi.org/https://doi.org/10.1016/j.jqsrt.2021.107949, 2021.

Hmiel, B., Petrenko, V. V., Dyonisius, M. N., Buizert, C., Smith, A. M., Place, P. F., Harth, C., Beaudette, R., Hua, Q., Yang, B., Vimont, I., Michel, S. E., Severinghaus, J. P., Etheridge, D., Bromley, T., Schmitt, J., Faïn, X., Weiss, R. F., and Dlugokencky, E.: Preindustrial $^{14}CH_4$ indicates greater anthropogenic fossil CH_4 emissions, Nature, 578, 409–412, https://doi.org/10.1038/s41586-020-1991-8, 2020.

Humpage, N., Boesch, H., Palmer, P. I., Vick, A., Parr-Burman, P., Wells, M., Pearson, D., Strachan, J., and Bezawada, N.: GreenHouse gas Observations of the Stratosphere and Troposphere (GHOST): an airborne shortwave-infrared spectrometer for remote sensing of greenhouse gases, Atmospheric Measurement Techniques, 11, 5199–5222, https://doi.org/10.5194/amt-11-5199-2018, 2018.

Karman, T., Koenis, M. A. J., Banerjee, A., Parker, D. H., Gordon, I. E., van der Avoird, A., van der Zande, W. J., and Groenenboom, G. C.: O2-O2 and O2-N2 collision-induced absorption mechanisms unravelled, Nature Chemistry, 10, 549–554, https://doi.org/10.1038/s41557-018-0015-x, 2018.

Karman, T., Gordon, I. E., van der Avoird, A., Baranov, Y. I., Boulet, C., Drouin, B. J., Groenenboom, G. C., Gustafsson, M., Hartmann, J.-M., Kurucz, R. L., Rothman, L. S., Sun, K., Sung, K., Thalman, R., Tran, H., Wishnow, E. H., Wordsworth, R., Vigasin, A. A., Volkamer, R., and van der Zande, W. J.: Update of the HITRAN collision-induced absorption section, Icarus, 328, 160–175, https://doi.org/https://doi.org/10.1016/j.icarus.2019.02.034, 2019.

Kleipool, Q., Ludewig, A., Babic, L. a., Bartstra, R., Braak, R., Dierssen, W., Dewitte, P. J., Kenter, P., Landzaat, R., Leloux, J., Loots, E., Meijering, P., Van Der Plas, E., Rozemeijer, N., Schepers, D., Schiavini, D., Smeets, J., Vacanti, G., Vonk, F., and Veefkind, P.: Pre-launch calibration results of the TROPOMI payload on-board the Sentinel-5 Precursor satellite, vol. 11, https://doi.org/10.5194/amt-11-6439-2018, 2018.

Konefał, M., Kassi, S., Mondelain, D., and Campargue, A.: High sensitivity spectroscopy of the O2 band at 1.27 μm: (I) pure O2 line parameters above 7920 cm^{-1}, Journal of Quantitative Spectroscopy and Radiative Transfer, 241, 1–12, https://doi.org/10.1016/j.jqsrt.2019.106653, 2020.

Kowalewski, M. G. and Janz, S. J.: Remote sensing capabilities of the Airborne Compact Atmospheric Mapper, 7452, 225 – 234, https://doi.org/10.1117/12.827035, 2009.

Kuze, A., Suto, H., Shiomi, K., Kataoka, F., Kawashima, T., Oda, T., Fujinawa, T., Kanaya, Y., and Tanimoto, H.: City-level CO2, CH4, and NO2 observations from Space: Airborne model demonstration over Nagoya, Earth and Space Science Open Archive, p. 1, https://doi.org/10.1002/essoar.10502004.1, 2020.

Lamsal, L. N., Janz, S. J., Krotkov, N. A., Pickering, K. E., Spurr, R. J. D., Kowalewski, M. G., Loughner, C. P., Crawford, J. H., Swartz, W. H., and Herman, J. R.: High-resolution NO_2 observations from the Airborne Compact Atmospheric Mapper: Retrieval and validation, Journal of Geophysical Research: Atmospheres, 122, 1953–1970, https://doi.org/https://doi.org/10.1002/2016JD025483, 2017.

Leitch, J. W., Delker, T., Good, W., Ruppert, L., Murcray, F., Chance, K., Liu, X., Nowlan, C., Janz, S. J., Krotkov, N. A., Pickering, K. E., Kowalewski, M., and Wang, J.: The GeoTASO airborne spectrometer project, 9218, 487 – 495, https://doi.org/10.1117/12.2063763, 2014.

Liu, C., Liu, X., Kowalewski, M. G., Janz, S. J., González Abad, G., Pickering, K. E., Chance, K., and Lamsal, L. N.: Characterization and verification of ACAM slit functions for trace-gas retrievals during the 2011 DISCOVER-AQ flight campaign, Atmospheric Measurement Techniques, 8, 751–759, https://doi.org/10.5194/amt-8-751-2015, 2015.

Maté, B., Lugez, C., Fraser, G. T., and Lafferty, W. J.: Absolute intensities for the O2 1.27 μm continuum absorption, Journal of Geophysical Research: Atmospheres, 104, 30 585–30 590, https://doi.org/https://doi.org/10.1029/1999JD900824, 1999.

MethaneSAT LLC: https://www.methanesat.org/fit-with-other-missions/, accessed: 2021-03-16.

545 Miller, C. E. and Wunch, D.: Fourier transform spectrometer remote sensing of O2 A-band electric quadrupole transitions, Journal of Quantitative Spectroscopy and Radiative Transfer, 113, 1043–1050, https://doi.org/https://doi.org/10.1016/j.jqsrt.2012.01.002, three Leaders in Spectroscopy, 2012.

NCAR - Earth Observing Laboratory: NSF/NCAR GV HIAPER Aircraft. UCAR/NCAR - Earth Observing Laboratory, https://doi.org/https://doi.org/10.5065/D6DR2SJP, retrieved December 14, 2016, 2005.

550 Nisbet, E. G., Manning, M. R., Dlugokencky, E. J., Fisher, R. E., Lowry, D., Michel, S. E., Myhre, C. L., Platt, S. M., Allen, G., Bousquet, P., Brownlow, R., Cain, M., France, J. L., Hermansen, O., Hossaini, R., Jones, A. E., Levin, I., Manning, A. C., Myhre, G., Pyle, J. A., Vaughn, B. H., Warwick, N. J., and White, J. W. C.: Very Strong Atmospheric Methane Growth in the 4 Years 2014–2017: Implications for the Paris Agreement, Global Biogeochemical Cycles, 33, 318–342, https://doi.org/https://doi.org/10.1029/2018GB006009, 2019.

NOAA: https://research.noaa.gov/article/ArtMID/587/ArticleID/2742/Despite-pandemic-shutdowns-carbon-dioxide-and-methane-surged-in-2020, 555 accessed: 2021-04-28, 2021.

Nowlan, C. R., Liu, X., Leitch, J. W., Chance, K., González Abad, G., Liu, C., Zoogman, P., Cole, J., Delker, T., Good, W., Murcray, F., Ruppert, L., Soo, D., Follette-Cook, M. B., Janz, S. J., Kowalewski, M. G., Loughner, C. P., Pickering, K. E., Herman, J. R., Beaver, M. R., Long, R. W., Szykman, J. J., Judd, L. M., Kelley, P., Luke, W. T., Ren, X., and Al-Saadi, J. A.: Nitrogen dioxide observations from the Geostationary Trace gas and Aerosol Sensor Optimization (GeoTASO) airborne instrument: Retrieval algorithm and measurements during 560 DISCOVER-AQ Texas 2013, Atmospheric Measurement Techniques, 9, 2647–2668, https://doi.org/10.5194/amt-9-2647-2016, 2016.

Nowlan, C. R., Liu, X., Janz, S. J., Kowalewski, M. G., Chance, K., Follette-Cook, M. B., Fried, A., González Abad, G., Herman, J. R., Judd, L. M., Kwon, H.-A., Loughner, C. P., Pickering, K. E., Richter, D., Spinei, E., Walega, J., Weibring, P., and Weinheimer, A. J.: Nitrogen dioxide and formaldehyde measurements from the GEOstationary Coastal and Air Pollution Events (GEO-CAPE) Airborne Simulator over Houston, Texas, Atmospheric Measurement Techniques, 11, 5941–5964, https://doi.org/10.5194/amt-11-5941-2018, 2018.

565 Pandey, S., Gautam, R., Houweling, S., van der Gon, H. D., Sadavarte, P., Borsdorff, T., Hasekamp, O., Landgraf, J., Tol, P., van Kempen, T., Hoogeveen, R., van Hees, R., Hamburg, S. P., Maasakkers, J. D., and Aben, I.: Satellite observations reveal extreme methane leakage from a natural gas well blowout, Proceedings of the National Academy of Sciences, 116, 26 376–26 381, https://doi.org/10.1073/pnas.1908712116, 2019.

Souri, A. H.: GEOAkaze, https://doi.org/10.5281/zenodo.6993473, 2022.

570 Staebell, C., Sun, K., Samra, J., Franklin, J., Chan Miller, C., Liu, X., Conway, E., Chance, K., Milligan, S., and Wofsy, S.: Spectral calibration of the MethaneAIR instrument, Atmospheric Measurement Techniques, 14, 3737–3753, https://doi.org/10.5194/amt-14-3737-2021, 2021.

Sun, K., Liu, X., Huang, G., González Abad, G., Cai, Z., Chance, K., and Yang, K.: Deriving the slit functions from OMI solar observations and its implications for ozone-profile retrieval, Atmospheric Measurement Techniques, 10, 3677–3695, https://doi.org/10.5194/amt-10-3677-2017, 2017a.

575 Sun, K., Liu, X., Nowlan, C. R., Cai, Z., Chance, K., Frankenberg, C., Lee, R. A., Pollock, R., Rosenberg, R., and Crisp, D.: Characterization of the OCO-2 instrument line shape functions using on-orbit solar measurements, Atmospheric Measurement Techniques, 10, 939–953, https://doi.org/10.5194/amt-10-939-2017, 2017b.

Sun, K., Gordon, I. E., Sioris, C. E., Liu, X., Chance, K., and Wofsy, S. C.: Reevaluating the Use of O_2 $a^1 \Delta g$ Band in Spaceborne Remote Sensing of Greenhouse Gases, Geophysical Research Letters, 45, 5779–5787, https://doi.org/https://doi.org/10.1029/2018GL077823, 580 2018.

Thompson, D. R., Thorpe, A. K., Frankenberg, C., Green, R. O., Duren, R., Guanter, L., Hollstein, A., Middleton, E., Ong, L., and Ungar, S.: Space-based remote imaging spectroscopy of the Aliso Canyon CH4 superemitter, Geophysical Research Letters, 43, 6571–6578, https://doi.org/https://doi.org/10.1002/2016GL069079, 2016.

585 Tol, P. J. J., van Kempen, T. A., van Hees, R. M., Krijger, M., Cadot, S., Snel, R., Persijn, S. T., Aben, I., and Hoogeveen, R. W. M.: Characterization and correction of stray light in TROPOMI-SWIR, Atmospheric Measurement Techniques, 11, 4493–4507, https://doi.org/10.5194/amt-11-4493-2018, 2018.

Tran, D., Tran, H., Vasilchenko, S., Kassi, S., Campargue, A., and Mondelain, D.: High sensitivity spectroscopy of the O_2 band at 1.27 μm: (II) air-broadened line profile parameters, Journal of Quantitative Spectroscopy and Radiative Transfer, 240, https://doi.org/10.1016/j.jqsrt.2019.106673, 2020.

590 Turner, A. J., Frankenberg, C., and Kort, E. A.: Interpreting contemporary trends in atmospheric methane, Proceedings of the National Academy of Sciences, 116, 2805–2813, https://doi.org/10.1073/pnas.1814297116, 2019.

van Hees, R. M., Tol, P. J. J., Cadot, S., Krijger, M., Persijn, S. T., van Kempen, T. A., Snel, R., Aben, I., and Hoogeveen: Determination of the TROPOMI-SWIR instrument spectral response function, Atmospheric Measurement Techniques, 11, 3917–3933, https://doi.org/10.5194/amt-11-3917-2018, 2018.

595 Van Kempen, T. A., Van Hees, R. M., Tol, P. J., Aben, I., and Hoogeveen, R. W.: In-flight calibration and monitoring of the Tropospheric Monitoring Instrument (TROPOMI) short-wave infrared (SWIR) module, Atmospheric Measurement Techniques, 12, 6827–6844, https://doi.org/10.5194/amt-12-6827-2019, 2019.

Veefkind, J., Aben, I., McMullan, K., Förster, H., de Vries, J., Otter, G., Claas, J., Eskes, H., de Haan, J., Kleipool, Q., van Weele, M., Hasekamp, O., Hoogeveen, R., Landgraf, J., Snel, R., Tol, P., Ingmann, P., Voors, R., Kruizinga, B., Vink, R.,

600 Visser, H., and Levelt, P.: TROPOMI on the ESA Sentinel-5 Precursor: A GMES mission for global observations of the atmospheric composition for climate, air quality and ozone layer applications, Remote Sensing of Environment, 120, 70–83, https://doi.org/https://doi.org/10.1016/j.rse.2011.09.027, the Sentinel Missions - New Opportunities for Science, 2012.

Voors, R., Dobber, M., Dirksen, R., and Levelt, P.: Method of calibration to correct for cloud-induced wavelength shifts in the Aura satellite's Ozone Monitoring Instrument, Appl. Opt., 45, 3652–3658, https://doi.org/10.1364/AO.45.003652, 2006.

605 Zhang, Y., Gautam, R., Pandey, S., Omara, M., Maasakkers, J. D., Sadavarte, P., Lyon, D., Nesser, H., Sulprizio, M. P., Varon, D. J., Zhang, R., Houweling, S., Zavala-Araiza, D., Alvarez, R. A., Lorente, A., Hamburg, S. P., Aben, I., and Jacob, D. J.: Quantifying methane emissions from the largest oil-producing basin in the United States from space, Science Advances, 6, https://doi.org/10.1126/sciadv.aaz5120, 2020.

Zoogman, P., Liu, X., Suleiman, R. M., Pennington, W. F., Flittner, D. E., Al-Saadi, J. A., Hilton, B. B., Nicks, D. K., Newchurch, M. J., Carr, J. L., Janz, S. J., Andraschko, M. R., Arola, A., Baker, B. D., Canova, B. P., Miller, C. C., Cohen, R. C., Davis, J. E., Dussault, M. E.,

610 Edwards, D. P., Fishman, J., Ghulam, A., Abad, G. G., Grutter, M., Herman, J. R., Houck, J., Jacob, D. J., Joiner, J., Kerridge, B. J., Kim, J., Krotkov, N. A., Lamsal, L., Li, C., Lindfors, A., Martin, R. V., McElroy, C. T., McLinden, C., Natraj, V., Neil, D. O., Nowlan, C. R., O'Sullivan, E. J., Palmer, P. I., Pierce, R. B., Pippin, M. R., Saiz-Lopez, A., Spurr, R. J. D., Szykman, J. J., Torres, O., Veefkind, J. P., Veihelmann, B., Wang, H., Wang, J., and Chance, K.: Tropospheric emissions: Monitoring of pollution (TEMPO), Journal of Quantitative Spectroscopy and Radiative Transfer, 186, 17–39, https://doi.org/10.1016/j.jqsrt.2016.05.008, 2017.